nature geoscience

ARTICLES

https://doi.org/10.1038/s41561-018-0242-1

Climatic and volcanic forcing of tropical belt northern boundary over the past 800 years

R. Alfaro-Sánchez[1,2*], H. Nguyen[3], S. Klesse[2], A. Hudson[2], S. Belmecheri[2], N. Köse[4], H. F. Diaz[5], R. K. Monson[2,6], R. Villalba[7] and V. Trouet[2]

The position of the northern boundary of the tropical belt affects the hydroclimate of many arid and semi-arid regions in the Northern Hemisphere. Widening of the tropical belt since the 1970s has largely been attributed to anthropogenic forcing. However, the relative influence of natural drivers of tropical belt expansion and contraction before this time is poorly understood. Here we use data on tree-ring widths from five mid-latitude regions in the Northern Hemisphere to reconstruct the movement of the northern boundary of the early spring tropical belt over the past 800 years (AD 1203–2003). Our reconstruction explains 45% of the interannual variance in the latitudinal extent of the Hadley circulation, a metric of the position of the tropical belt boundary. We find that the tropical belt contracted (expanded) during positive (negative) phases of the El Niño Southern Oscillation and Pacific North American teleconnection patterns. The tropical belt also contracted significantly following major volcanic events that injected sulfur into the stratosphere. The longest period of persistent tropical belt expansion occurred in the late sixteenth century, during one of the coldest periods of the Little Ice Age. Our results warn of potential socio-economic consequences of future variations in tropical belt width driven by natural climate variability or stratospheric aerosol injections, whether volcanic or artificial.

The boundaries of the tropical belt—climatologically identified on the basis of a range of climatological metrics, including the extent of the Hadley circulation—determine the latitude of the subtropical dry zone[1]. Latitudinal movements of the tropical belt boundary influence the hydroclimate in many arid and semi-arid regions, and are critical for sustainable use of urban resources, regional agriculture and ecosystem water services[2].

On seasonal and interannual timescales, the position of the tropical belt boundary is associated with external forcings such as volcanic activity, as well as with internal climate variability[3], including tropical–extratropical teleconnections, such as the Pacific North America (PNA) pattern[4] and the El Niño Southern Oscillation (ENSO) system[5]. On multidecadal timescales, the Pacific Decadal Oscillation (PDO)[6] and the northern and southern annular modes[7] can influence tropical belt variations.

Since the late 1970s, the tropical belt has shown a poleward expansion in both hemispheres[8], which is associated with changing global precipitation patterns and has encouraged a suite of observational, reanalysis and modelling studies investigating the Earth system mechanisms and forcings that drive shifts in tropical belt width[1,3].

The magnitude of the observed poleward shift in the late twentieth century is dependent on the data and metrics used[8]. Reanalysis products tend to agree on the Northern Hemisphere tropical expansion[7] and to amplify it compared with model simulations[8,9], even when the magnitude of the expansion is less pronounced in most recent reanalysis products compared to earlier ones[9].

Historical general circulation model (GCM) runs indicate that the observed widening over the twenty-first century may result from combined greenhouse gas (GHG) forcing[1,3,10], black carbon aerosols and tropospheric ozone in the Northern Hemisphere[11,12], and stratospheric ozone depletion in the Southern Hemisphere[13]. In the Northern Hemisphere mid-latitudes, this recent tropical expansion has been partly offset by increasing industrial aerosol (for example sulfate) emissions that cause tropospheric cooling[12].

However, coupled climate model simulations show no clear consensus on the primary forcing mechanism of Northern Hemisphere tropical expansion over the past four decades[8], and comparisons of models with observations show that neither anthropogenic forcing[14] nor natural variability[15,16] alone can explain it. As a result, the relative importance of anthropogenic versus natural drivers is incompletely understood[10,11]. The drivers of an observed multidecadal 1945–1980 contraction of the Northern Hemisphere tropical belt[8,17] are even less well known.

Such shortcomings in our understanding of the factors influencing the tropical belt width can lead to a large intermodel spread in simulated future trends[18], and thus to large uncertainties in future hydroclimate projections. Advanced models and more refined observations are needed to reduce such uncertainties and to improve the ability of GCMs to project trends in tropical belt width. This information will provide a better understanding of the relative roles of prospective drivers, particularly aerosols[1,11]. Here, we contribute to this by using data on tree-ring widths to reconstruct the northern boundary of the tropical belt over the past 800 years (AD 1203–2003).

The target of our reconstruction is the latitudinal extent of the Hadley circulation (HCE), a commonly used metric that is robust in its representation of the position of the tropical belt boundary[7,19]. We computed monthly HCE indices for the period AD 1930–2014, averaged over all longitudes in the Northern Hemisphere, based on

[1]Centre de Recerca Ecològica i Aplicacions Forestals (CREAF), Barcelona, Spain. [2]Laboratory of Tree-Ring Research, University of Arizona, Tucson, AZ, USA. [3]Bureau of Meteorology, Melbourne, Victoria, Australia. [4]Istanbul University-Cerrahpaşa, Forestry Faculty, Forest Botany Department, Bahçeköy-Istanbul, Turkey. [5]Department of Geography and Environment, University of Hawai'i at Mānoa, Honolulu, USA. [6]Department of Ecology and Evolutionary Biology, University of Arizona, Tucson, AZ, USA. [7]Instituto Argentino de Nivología, Glaciología y Ciencias Ambientales (IANIGLA–CONICET), Mendoza, Argentina. *e-mail: r.alfarosanchez@gmail.com

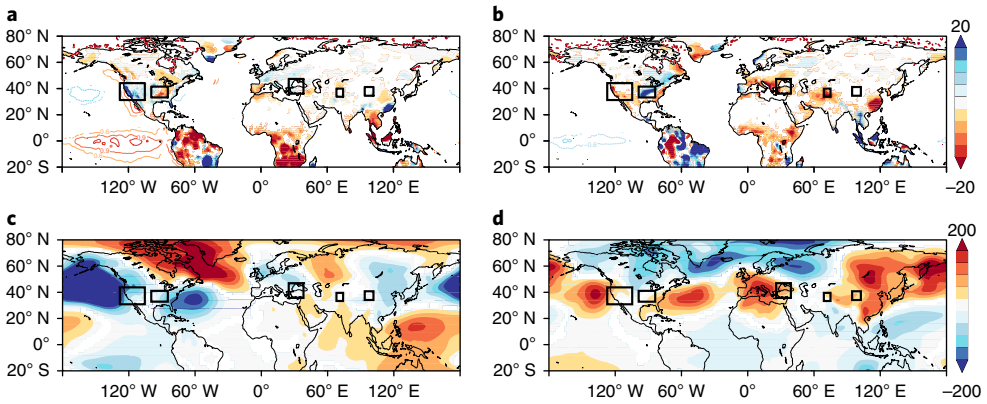

Fig. 1 | Influence of February to April HCE_{FMA} on Northern Hemisphere climate variability. a,**b**, Composite maps of anomalies in FMA precipitation from the Climatic Research Unit time series CRU TS4.01 (shading every 4 mm — top colour scale) and in SSTs from HadISST1 (contours every 0.3 °C) for the 10th percentile (southernmost) (**a**) and 90th percentile (northernmost) (**b**) HCE_{FMA} years (AD 1930–2014, $P<0.05$), with blue (and red) colours indicating wet and cool (and dry and warm) anomalies, respectively. **c**,**d**, Composite maps of FMA sea-level pressure from the Twentieth Century Reanalysis V2 for the 10th percentile (southernmost) (**c**) and 90th percentile (northernmost) (**d**) HCE_{FMA} years (shading every 40 Pa — bottom colour scale; AD 1930–2011, $P<0.05$). Black boxes in each panel indicate the locations of the five regional chronologies used in the reconstruction models.

meridional winds derived from the Twentieth Century Reanalysis V2 (20CR) dataset[20] according to the method described in ref. [21] and modified by ref. [22] (Supplementary Fig. 1; see Methods).

Northern or southern HCE excursions, particularly during early spring (FMA: February, March and April), can have a considerable impact on precipitation patterns near the northern edge of the subtropical region (~35–40° N), and precipitation-sensitive tree-ring data from these locations can thus reflect HCE_{FMA} movements (Fig. 1). We used mid-latitude tree-ring width data that are sensitive to precipitation or water deficit (for example the self-calibrating Drought Severity Index, scPDSI) during the target season (FMA) to compile regional tree-ring chronologies for five Northern Hemisphere regions (Supplementary Tables 1 and 2; Methods). The five regions of the Northern Hemisphere are located in western and central North America (hereafter W USA and C USA), southeastern Europe (Turkey, hereafter E EU), and western and central Asia (northern Pakistan, hereafter W Asia; and the Tibetan Plateau, hereafter C Asia; Fig. 1). Fluctuations in intensity of the FMA Northern Hemisphere Hadley circulation (hereafter HCI_{FMA}; see Methods) can also affect subtropical precipitation patterns, particularly in W USA and C Asia (Supplementary Fig. 2). However, the five regional tree-ring chronologies, and 93 out of the 96 site chronologies contributing to them, are independent of HCI_{FMA} variability (Supplementary Tables 1 and 3a), and we therefore consider our reconstruction to reflect primarily variations in HCE_{FMA}.

We developed two regression models to reconstruct HCE_{FMA} based on these five regional tree-ring chronologies. The first model includes all five regional chronologies and extends back over their common period (AD 1532–2003). The second model includes three chronologies (W USA, C USA and C Asia) that extend back to AD 1203 and was used to reconstruct HCE_{FMA} for the period AD 1203–1531 (Fig. 2; Supplementary Fig. 3). Both models are calibrated against a reanalysis-based HCE_{FMA} target[20] over their period of overlap (AD 1930–2003), explain 51% and 45% of the total variance in that target, respectively, and show robust statistical skills (Supplementary Table 3). The five-chronology model and the three-chronology model were merged to obtain the reconstruction of the early spring northern boundary of the tropical belt ($RHCE_{FMA}$) covering the period AD 1203–2003.

Internal climate variability

Our reanalysis-based HCE_{FMA} target is significantly negatively correlated with the leading modes of sea surface temperature (SST) variability: ENSO (AD 1930–2014, $r=-0.60$, $P<0.001$, for the eastern Pacific FMA NIÑO3.4 SST, and $r=-0.52$, $P<0.001$, for the central Pacific FMA NIÑO4 SST) and PDO (AD 1930–2014, $r=-0.41$, $P<0.001$). This coupling is reflected by the warmer (cooler) SSTs found in the tropical Pacific during southernmost (northernmost) HCE_{FMA} positions (Fig. 1a,b). Our results thus confirm that over the instrumental period (AD 1930–2014), the early spring tropical belt boundary in the Northern Hemisphere tends to contract (expand) during the warm (cool) phases of ENSO and PDO, triggered by an increase (decrease) in the meridional temperature gradient[5,6,9,21].

Pacific SSTs also modulate PNA phases, with positive (negative) PNA phases associated with warm (cool) phases of ENSO and PDO[23]. As such, our HCE_{FMA} target also correlates significantly negatively with the FMA PNA pattern (AD 1950–2014, $r=-0.56$, $P<0.001$). Composite maps of February-to-April sea level pressure (SLP) for southernmost (northernmost) HCE_{FMA} positions reflect the positive (negative) phase of the PNA teleconnection pattern (Fig. 1c,d).

In line with our findings for the twentieth and twenty-first centuries, the early spring tropical belt boundary in the Northern Hemisphere (AD 1203–2003)—here represented by the reconstructed FMA Hadley circulation extent ($RHCE_{FMA}$) — typically moved southward during warm ENSO (El Niño) and positive PNA phases and northward during cold ENSO (La Niña) and negative PNA phases over the past 800 years. These $RHCE_{FMA}$–ENSO and $RHCE_{FMA}$–PNA relationships are reflected in the significantly negative correlations between $RHCE_{FMA}$ and two ENSO reconstructions and one PNA reconstruction over their full period of overlap ($r=-0.20$, $P<0.001$ with NIÑO3.4[24] (AD 1301–2003); $r=-0.12$, $P<0.001$ with NIÑO4[25] (AD 1203–2003); $r=-0.20$, $P<0.001$ with PNA[26] (AD 1203–1998)). $RHCE_{FMA}$ movements during past positive (negative) ENSO and PNA extremes, defined as the 95th and 90th (5th and 10th) percentiles of the reconstructions[24–26], are further demonstrated in a superposed epoch analysis (SEA; see Methods). We found a significant contraction of the $RHCE_{FMA}$ during extreme positive ENSO (El Niño) and PNA phases and a significant expansion during extreme negative ENSO (La Niña) and PNA phases (Fig. 3a–c). These results are confirmed by a reverse SEA that composites reconstructed ENSO and PNA indices during southernmost and northernmost $RHCE_{FMA}$ extremes (Supplementary Fig. 4).

Spectral analyses revealed significant periodicity in the position of the $RHCE_{FMA}$ within interannual (3–8 years) and decadal (10–26 years) bands over the past eight centuries (Supplementary

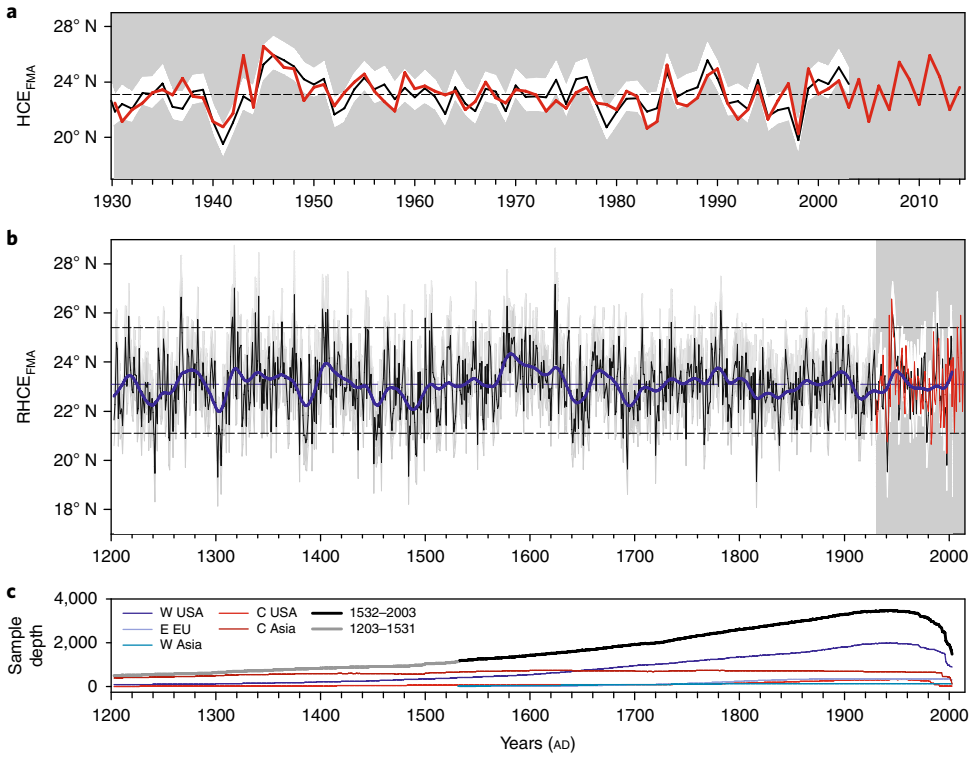

Fig. 2 | Reconstruction of the early spring northern boundary of the tropical belt. a, **b**, Annually resolved instrumental (red line, HCE$_{FMA}$) and reconstructed (black line, RHCE$_{FMA}$) February–April Hadley circulation extent in degrees of latitude for the AD 1930–2014 instrumental period (**a**) and the AD 1203–2003 period (**b**). In **b**, the blue line represents the 30-year low-pass-filtered RHCE$_{FMA}$, and dashed horizontal lines indicate the average, 5th and 95th percentile positions of RHCE$_{FMA}$. Shading around the reconstruction represents the combined chronology and calibration error estimation. **c**, Sample depth over time for each of the five master chronologies and for the periods AD 1532–2003 and AD 1203–1531.

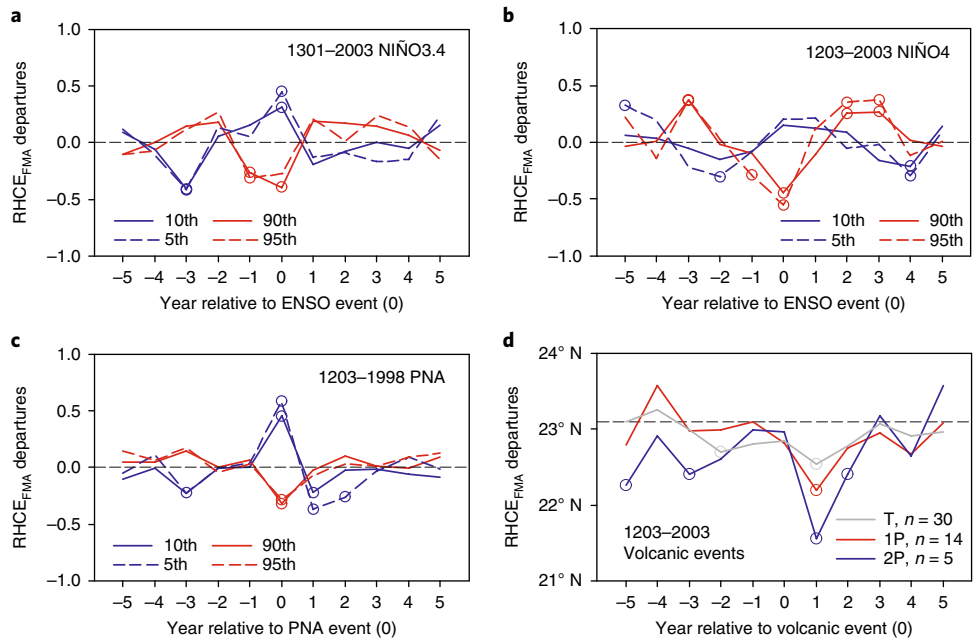

Fig. 3 | RHCE$_{FMA}$ response to ENSO and PNA extremes and to major volcanic events. a–c, SEAs showing RHCE$_{FMA}$ anomalies during extreme negative (positive) El Niño Southern Oscillation (ENSO) and Pacific-North American years, defined as the 5th and 10th (95th and 90th) percentiles of two ENSO reconstructions, NIÑO3.4 SST[24] (**a**) and NIÑO4 SST[25] (**b**), and one PNA reconstruction[26] (**c**). **d**, SEA showing the RHCE$_{FMA}$ response in degrees of latitude to tropical volcanic events (T) and events the same size as Pinatubo (1P) or twice as large (2P), based on a revised volcanic forcing reconstruction[29]. Significant ($P < 0.05$) departures are indicated by circles. The list of the events is in Supplementary Tables 4 and 6.

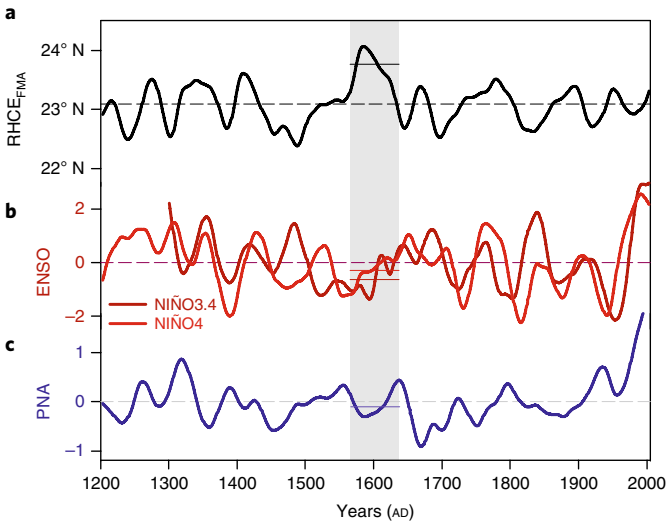

Fig. 4 | Variability in the tropical belt northern boundary, El Niño Southern Oscillation (ENSO) and Pacific-North American (AD 1203–2003). **a**–**c**, Fifty-year smoothed time series of reconstructed latitudinal position of the RHCE$_{FMA}$ (**a**), winter NIÑO3.4[24] and spring NIÑO4[25] SSTs (**b**), and winter PNA anomalies[26] (**c**). Grey shaded area indicates a period of persistent tropical belt expansion, and horizontal lines inside this area indicate the average position of the reconstructions.

Fig. 5; Fig. 2), highlighting the association between the RHCE$_{FMA}$ movements and past ENSO[24], PNA and PDO variability[27].

Post-volcanic tropical belt contractions

Past GCM simulations have shown that the northern boundary of the tropical belt is projected to contract after major volcanic stratospheric sulfur injection events[16]. Reanalysis data have also shown that increases in stratospheric volcanic aerosols drive a weakening and equatorward shift of the subtropical jet, and the associated HCE[28], but direct observational evidence of past post-volcanic tropical belt contractions is lacking.

Volcanic sulfate aerosol injections into the stratosphere block the Earth's surface from incoming solar radiation driving cooling at regional-to-global scales that can persist for up to 10 years (ref. [29]), along with changes in atmospheric circulation and precipitation patterns that can persist for up to 2 years (refs [30,31]).

The tropical eruption of Mount Tambora in 1815, for instance, resulted in the following year 1816 being one of the coolest years recorded for the Northern Hemisphere[32], often referred to as 'the year without summer'[33]. Our reconstruction shows that the RHCE$_{FMA}$ in 1816 was in its southernmost position for at least the past 800 years.

To put the 1816 contraction of the Northern Hemisphere tropical belt into a longer-term context, we applied SEA to determine the response of RHCE$_{FMA}$ to past major volcanic forcing events (AD 1203–2003). These major volcanic events were defined as: (1) tropical volcanic events and (2) events with sulfate injections the same size as the 1991 eruption of Pinatubo (1P) or twice the size (2P), derived from three independent, ice-core-based volcanic reconstructions (see Methods and Supplementary Table 4). We found evidence of a significant contraction of 0.25° to 0.86° latitude, one year after tropical events, and stronger contractions of 0.41° to 0.99° and 1.25° to 1.56°, one year after 1P and 2P volcanic events, respectively (Fig. 3d; Supplementary Fig. 6a,b).

We also used SEA to detect post-volcanic effects in the five individual mid-latitude regional chronologies contributing to RHCE$_{FMA}$. We found significant positive post-volcanic responses in tree growth for the W USA and E EU chronologies (Supplementary Fig. 6c–e). The observed increases in tree growth are related to the wet conditions following volcanic events reported for both regions[31], similar to the positive precipitation anomalies caused by southern HCE positions (Fig. 1a).

Observational data and model simulations have linked the onset of El Niño (positive ENSO phases) to large tropical or Northern Hemisphere eruptions[25,34]. This is consistent with our results showing significant contractions of the RHCE$_{FMA}$ in response to El Niño events (Fig. 3a,b), which in turn occur up to 2 years following volcanic events (Fig. 3d). Such an El Niño-amplified response can be expained by the thermostat mechanism in the equatorial Pacific[35]: the western Pacific warm pool is more sensitive to changes in radiative forcing than the eastern Pacific and will cool relatively faster following a uniform radiative reduction such as those associated with large volcanic events. As a result, the zonal SST gradient in the Pacific will initially decrease, and the trade winds driven by this gradient will weaken. These effects will, in turn, lead to a further reduction of the SST gradient, and promote the emergence of El Niño conditions[34].

Late sixteenth-century tropical belt expansion

The Little Ice Age (LIA)[36], a period from c. AD 1450 to 1850, was generally characterized by low atmospheric CO_2 concentrations, cooling in the Northern Hemisphere[36] and strong tropical volcanic activity (Supplementary Table 4). Low-resolution palaeoclimate records that accurately capture centennial-scale variability indicate that the LIA was generally characterized by El Niño-like conditions[37] and coincided with a contraction of the tropical belt[38] and a southward movement of the Intertropical Convergence Zone[39,40].

Our reconstruction is limited in its ability to capture the centennial-scale variability of the LIA. It best represents HCE$_{FMA}$ variability at interannual to decadal scales (Fig. 4a; Supplementary Fig. 5). On these decadal timescales, we find an expansion covering six decades that occurred during one of the coldest periods of the LIA. The longest period of persistent tropical belt expansion in RHCE$_{FMA}$ extended from c. AD 1568 to 1634, with a northernmost expansion peak in 1624 (Fig. 2b).

Several Northern Hemisphere regions where dry conditions prevail during HCE$_{FMA}$ expansions, such as the southwestern and southeastern United States, northern Mexico, Turkey and eastern China, are documented to have experienced the most severe droughts of at least the past 500 years at the end of the sixteenth century[41–43]. In particular, two extreme droughts during the period from AD 1587 to 1612 in the Carolinas and Virginia of the United States have been linked to the disappearance of the Lost Colony of Roanoke Island and the near-abandonment at Jamestown Colony, the first English settlements in North America[44].

In Turkey, the famine, rural flight, epidemics and violence associated with a severe 1590s drought gave rise to the Celâlî Rebellion (AD 1596–1610), the most severe crisis in Ottoman history before World War I. During the crisis, rebel armies plundered the Ottoman provinces in their revolt against the authority of the Ottoman Empire[45]. In Asia, the exceptional drought event that occurred in AD 1586–1589 over eastern China was followed by widespread famines and peasant rebellions that marked the end of the Ming dynasty, which finally collapsed in 1644[43].

Most of these severe droughts have been recorded as summer droughts in tree-ring-based palaeoclimate reconstructions that are independent of RHCE$_{FMA}$. They commonly targeted drought indices, such as scPDSI, that integrate short- to long-term effects on the soil water balance, and thus recorded drought conditions not only in summer, but also in the spring months leading up to it[41]. As such, a northward movement of the RHCE in early spring (FMA) during the late sixteenth century could have moved storm tracks away from these regions and created prolonged spring but also

summer drought conditions. The synchronicity of these historically documented societal crises over the Northern Hemisphere can thus be linked to the $RHCE_{FMA}$ expansion of the late sixteenth to early seventeenth century.

The driving force behind this period of persistent tropical belt expansion, however, is not fully understood. A recent climate model simulation for E EU, one of the regions impacted by HCE_{FMA} (Fig. 1a,b), suggests that internal climate dynamics, rather than external forcings, drove decadal-scale precipitation variability in the late sixteenth and early seventeenth centuries[45]. Such climate dynamical patterns, including ENSO and PDO, have also been linked to the extreme droughts across North America in the late sixteenth century[41].

In the late 1500s and early 1600s, ENSO was more negative than average[24,25] (Fig. 4b) and these La Niña-like conditions in the tropical Pacific could also have contributed to a negative PNA pattern[26] (Fig. 4c) and thus be in line with northward $RHCE_{FMA}$ positions (Fig.4a; Fig. 3a–c). It is likely that the tropical belt expansion of the late sixteenth to early seventeenth century was driven by internal climatic variability, rather than external forcings such as volcanic eruptions.

Role of anthropogenic forcing

Our $RHCE_{FMA}$ extends the observational period of interannual tropical belt movements in the Northern Hemisphere by more than 700 years and shows that before the twenty-first-century increases in GHG and anthropogenic aerosol emissions, natural atmospheric variability and volcanic forcing were the primary drivers of early spring tropical belt variations in the Northern Hemisphere.

Over the most recent four decades, our instrumental HCE_{FMA} target shows an expansion trend of 0.4° per decade (1979–2014; Supplementary Fig. 1c), which is consistent with other recent reanalysis-based expansion rates[1,5,9]. The correlation between HCE_{FMA} and FMA ENSO and PDO modes also increases over this period (AD 1979–2014, NIÑO3.4 SST $r=-0.71$; NIÑO4 SST $r=-0.6$; PDO $r=-0.61$, $P<0.001$), compared with an earlier period of similar length (AD 1943–1978, NIÑO3.4 $r=-0.3$ SST; NIÑO4 SST $r=-0.3$, $P<0.1$; PDO $r=-0.05$, $P>0.1$).

This strong relationship in recent decades suggests that anthropogenic forcing of internal climate modes[6], such as the recent increase in the frequency of La Niña events[46] and the post-1979 change of phase in the PDO[6], might amplify or temper projected twenty-first-century expansion of the Northern Hemisphere tropics due to increased GHG emissions and decreased aerosol emissions[47].

In closing, we show that, like anthropogenic aerosols[47], volcanic effects lead to a contraction of the $RHCE_{FMA}$. We find that past major volcanic events have resulted in a short-lived (1–2 year) contraction of the $RHCE_{FMA}$. Our results should be taken into account when considering the potential implications of proposed solar radiation management approaches. In view of delayed action on GHG emission reductions, continuous and deliberate injections of aerosols into the stratosphere (mimicking the effect of major volcanic eruptions) are increasingly being considered in an effort to counteract anthropogenic planetary warming[48]. Our results indicate that, in addition to modelled impacts on regional hydroclimate[49] and on extreme climate events[50], such artificial stratospheric aerosol injections could result in tropical belt contractions. These contractions could potentially offset projected GHG-driven tropical expansion[47], but can have hemispheric-scale hydroclimate implications that demand careful consideration.

Online content

Any methods, additional references, Nature Research reporting summaries, source data, statements of data availability and associated accession codes are available at https://doi.org/10.1038/s41561-018-0242-1.

Received: 14 February 2018; Accepted: 10 September 2018;
Published online: 15 October 2018

References

1. Seidel, D. J., Fu, Q., Randel, W. J. & Reichler, T. J. Widening of the tropical belt in a changing climate. *Nat. Geosci.* **1**, 21–24 (2008).
2. Seager, R. & Vecchi, G. A. Greenhouse warming and the 21st century hydroclimate of southwestern North America. *Proc. Natl Acad. Sci. USA* **107**, 21277–21282 (2010).
3. Lucas, C., Timbal, B. & Nguyen, H. The expanding tropics: a critical assessment of the observational and modeling studies. *Wiley Interdiscip. Rev. Clim. Change* **5**, 89–112 (2014).
4. Lucas, C. & Nguyen, H. Regional characteristics of tropical expansion and the role of climate variability. *J. Geophys. Res. Atmos.* **120**, 6809–6824 (2015).
5. Lu, J., Chen, G. & Frierson, D. M. W. Response of the zonal mean atmospheric circulation to El Niño versus global warming. *J. Clim.* **21**, 5835–5851 (2008).
6. Allen, R. J., Norris, J. R. & Kovilakam, M. Influence of anthropogenic aerosols and the Pacific Decadal Oscillation on tropical belt width. *Nat. Geosci.* **7**, 270–274 (2014).
7. Nguyen, H., Evans, A., Lucas, C., Smith, I. & Timbal, B. The Hadley circulation in reanalyses: climatology, variability, and change. *J. Clim.* **26**, 3357–3376 (2013).
8. D'Agostino, R. & Lionello, P. Evidence of global warming impact on the evolution of the Hadley circulation in ECMWF centennial reanalyses. *Clim. Dyn.* **48**, 3047–3060 (2017).
9. Adam, O., Schneider, T. & Harnik, N. Role of changes in mean temperatures versus temperature gradients in the recent widening of the hadley circulation. *J. Clim.* **27**, 7450–7461 (2014).
10. Hu, Y., Tao, L. & Liu, J. Poleward expansion of the Hadley circulation in CMIP5 simulations. *Adv. Atmos. Sci.* **30**, 790–795 (2013).
11. Allen, R. J., Sherwood, S. C., Norris, J. R. & Zender, C. S. Recent Northern Hemisphere tropical expansion primarily driven by black carbon and tropospheric ozone. *Nature* **485**, 350–354 (2012).
12. Wang, H., Xie, S.-P. & Liu, Q. Comparison of climate response to anthropogenic aerosol versus greenhouse gas forcing: distinct patterns. *J. Clim.* **29**, 5175–5188 (2016).
13. Polvani, L. M., Waugh, D. W., Correa, G. J. P. & Son, S.-W. Stratospheric ozone depletion: the main driver of twentieth-century atmospheric circulation changes in the Southern Hemisphere. *J. Clim.* **24**, 795–812 (2011).
14. Garfinkel, C. I., Waugh, D. W. & Polvani, L. M. Recent Hadley cell expansion: the role of internal atmospheric variability in reconciling modeled and observed trends. *Geophys. Res. Lett.* **42**, 10824–10831 (2015).
15. Johanson, C. M. & Fu, Q. Hadley cell widening: model simulations versus observations. *J. Clim.* **22**, 2713–2725 (2009).
16. Lu, J., Deser, C. & Reichler, T. Cause of the widening of the tropical belt since 1958. *Geophys. Res. Lett.* **36**, L03803 (2009).
17. Brönnimann, S. et al. Southward shift of the northern tropical belt from 1945 to 1980. *Nat. Geosci.* **8**, 969–974 (2015).
18. Davis, N. & Birner, T. On the discrepancies in tropical belt expansion between reanalyses and climate models and among tropical belt width metrics. *J. Clim.* **30**, 1211–1231 (2017).
19. Davis, N. & Birner, T. Climate model biases in the width of the tropical belt. *J. Clim.* **29**, 1935–1954 (2016).
20. Compo, G. P. et al. The twentieth century reanalysis project. *Q. J. R. Meteorol. Soc.* **137**, 1–28 (2011).
21. Oort, A. H. & Yienger, J. J. Observed interannual variability in the Hadley circulation and its connection to ENSO. *J. Clim.* **9**, 2751–2767 (1996).
22. Nguyen, H. et al. Variability of the extent of the Hadley circulation in the southern hemisphere: a regional perspective. *Clim. Dyn.* **50**, 129–142 (2018).
23. Horel, J. D. & Wallace, J. M. Planetary-scale atmospheric phenomena associated with the Southern Oscillation. *Mon. Weather Rev.* **109**, 813–829 (1981).
24. Li, J. et al. El Niño modulations over the past seven centuries. *Nat. Clim. Change* **3**, 822–826 (2013).
25. Liu, Y. et al. Recent enhancement of central Pacific El Niño variability relative to last eight centuries. *Nat. Commun.* **8**, 15386 (2017).
26. Liu, Z. et al. Pacific North American circulation pattern links external forcing and North American hydroclimatic change over the past millennium. *Proc. Natl Acad. Sci. USA* **114**, 3340 (2017).
27. D'Arrigo, R. & Wilson, R. On the Asian expression of the PDO. *Int. J. Climatol.* **26**, 1607–1617 (2006).
28. Haigh, J. D., Blackburn, M. & Day, R. The response of tropospheric circulation to perturbations in lower-stratospheric temperature. *J. Clim.* **18**, 3672–3685 (2005).
29. Sigl, M. et al. Timing and climate forcing of volcanic eruptions for the past 2,500 years. *Nature* **523**, 543–549 (2015).

30. Robock, A. Volcanic eruptions and climate. *Rev. Geophys.* **38**, 191–219 (2000).
31. Iles, C. E., Hegerl, G. C., Schurer, A. P. & Zhang, X. The effect of volcanic eruptions on global precipitation. *J. Geophys. Res. Atmos.* **118**, 8770–8786 (2013).
32. Wilson, R. et al. Last millennium Northern Hemisphere summer temperatures from tree rings. Part I: The long term context. *Quat. Sci. Rev.* **134**, 1–18 (2016).
33. Luterbacher, J. & Pfister, C. The year without a summer. *Nat. Geosci.* **8**, 246 (2015).
34. Emile-Geay, J., Seager, R., Cane, M. A., Cook, E. R. & Haug, G. H. Volcanoes and ENSO over the past millennium. *J. Clim.* **21**, 3134–3148 (2008).
35. Clement, A. C., Seager, R., Cane, M. A. & Zebiak, S. E. An ocean dynamical thermostat. *J. Clim.* **9**, 2190–2196 (1996).
36. Grove, J. *The Little Ice Age* (Methuen, London, 1988).
37. Mann, M. E. et al. Global signatures and dynamical origins of the Little Ice Age and medieval climate anomaly. *Science* **326**, 1256–1260 (2009).
38. Denniston, R. F. Expansion and contraction of the Indo-pacific tropical rain belt over the last three millennia. *Sci. Rep.* **6**, 34485 (2016).
39. Ridley, H. E. et al. Aerosol forcing of the position of the intertropical convergence zone since AD 1550. *Nat. Geosci.* **8**, 195–200 (2015).
40. Lechleitner, F. A. et al. Tropical rainfall over the last two millennia: evidence for a low-latitude hydrologic seesaw. *Sci. Rep.* **7**, 45809 (2017).
41. Stahle, D. W. et al. Tree-ring data document 16th century megadrought over North America. *Eos Trans. AGU* **81**, 121–125 (2000).
42. Touchan, R., Akkemik, Ü., Hughes, M. K. & Erkan, N. May–June precipitation reconstruction of southwestern Anatolia, Turkey during the last 900 years from tree rings. *Quat. Res.* **68**, 196–202 (2007).
43. Shen, C., Wang, W.-C., Hao, Z. & Gong, W. Exceptional drought events over eastern China during the last five centuries. *Clim. Change* **85**, 453–471 (2007).
44. Stahle, D. W., Cleaveland, M. K., Blanton, D. B., Therrell, M. D. & Gay, D. A. The lost colony and Jamestown droughts. *Science* **280**, 564 (1998).
45. Xoplaki, E. et al. Modelling climate and societal resilience in the eastern Mediterranean in the last millennium. *Hum. Ecol.* **46**, 363–379 (2018).
46. Cai, W. et al. Increased frequency of extreme La Niña events under greenhouse warming. *Nat. Clim. Change* **5**, 132–137 (2015).
47. Allen, R. J. & Ajoku, O. Future aerosol reductions and widening of the northern tropical belt. *J. Geophys. Res. Atmos.* **121**, 6765–6786 (2016).
48. Caldeira, K., Bala, G. & Cao, L. The science of geoengineering. *Annu. Rev. Earth. Planet. Sci.* **41**, 231–256 (2013).
49. Ricke, K. L., Morgan, M. G. & Allen, M. R. Regional climate response to solar-radiation management. *Nat. Geosci.* **3**, 537 (2010).
50. Jones, A. C. et al. Impacts of hemispheric solar geoengineering on tropical cyclone frequency. *Nat. Commun.* **8**, 1382 (2017).

Acknowledgements

This study was supported by the US National Science Foundation (NSF) CAREER grant AGS-1349942 and the NSF grant 1065790 from the Emerging Frontiers Section in the Division of Environmental Biology. R.A.S. is supported by the postdoctoral grant Juan de la Cierva-Formación-FJCI-2015-26848, from the Spanish Ministry of Economy, Industry and Competitiveness. S.K. acknowledges the support of USDA-AFRI grant 2016-67003-24944. R.K.M. acknowledges support from NSF Ecosystems Program grant 1754430. R.V. is partially supported by the BNP-PARIBAS Foundation.

Author contributions

V.T., R.V. and R.A.S. conceived and designed the research. R.A.S. led the analysis and figure preparation and wrote the manuscript, with major contributions by V.T. and H.N. H.N. provided the monthly Hadley circulation indices data for the northern hemisphere. S.K. and A.H. contributed to data analysis. N.K. provided tree-ring chronologies. V.T. and R.K.M. organized financial support. All authors contributed to scientific discussions and to the preparation of the manuscript.

Additional information

Supplementary information is available for this paper at https://doi.org/10.1038/s41561-018-0242-1.

Reprints and permissions information is available at www.nature.com/reprints.

Correspondence and requests for materials should be addressed to R.A.

Publisher's note: Springer Nature remains neutral with regard to jurisdictional claims in published maps and institutional affiliations.

Methods

Hadley circulation. Our reconstruction targets the HCE as a metric for the tropical belt extent in the Northern Hemisphere. Monthly HCE indices, averaged over all longitudes of the Northern Hemisphere, were computed according to ref. [21] modified by ref. [22]. The modification consists of computing the zonal mean stream function for meridional mass from the zonal mean divergent component of the meridional wind instead of directly from the zonal mean meridional wind. We first decomposed monthly horizontal winds into the divergent components in spherical coordinates, which is the only part of the wind that contributes to the vertical motion and can be regarded as the meridional overturning circulation. The global (zonal mean) mass stream function was computed from the monthly divergent meridional wind component in the same way as ref. [21]. The HCE is defined as the average position of the 25%-peak value of the global stream function between 400 and 700 hPa. The results of our methodology agree with the classical definition described in ref. [21], with correlations exceeding 0.9 when comparing zonal mean edges of the Hadley circulation[22,51].

HCE indices were based on horizontal wind data derived from the Twentieth Century Reanalysis V2 (20CR) dataset[20]. The 20CR dataset is available from 1871 to present, with a spatial resolution of 2° and a monthly temporal resolution. We limited the monthly target time series to the period AD 1930–2014 because 20CR can be strongly affected by inhomogeneity in its earliest period, owing to a decline in station density and measurement quality[52], particularly before the arrival of radiosonde measurements in the 1930s[20].

We used monthly HCI indices, defined by the maximum values of the overturning stream function expressed in kg s^{-1} and derived from the 20CR dataset[20], to study the intra-seasonal variability of HCI and its association with HCE position. The Hadley circulation, which is thermally driven, responds to increased global temperatures by decreasing its intensity and increasing its latitudinal extension[5,7]. Our analysis confirmed previous reanalysis results[6] suggesting that HC strengthens and contracts during winter and early spring, and weakens and expands during summer in the 20CR dataset, but the intra-annual peak of the northernmost HCE position is slightly out of phase with the weakest HCI (Supplementary Fig. 1a). During early spring (FMA), the Northern Hemisphere HCE (hereafter HCE_{FMA}) is relatively close to the Equator, while FMA Northern Hemisphere HCI (hereafter HCI_{FMA}) is relatively high (Supplementary Fig. 1a), and HCI_{FMA} and HCE_{FMA} time series are inversely correlated with each other (AD 1930–2008; $r=-0.38$, $P<0.001$; Supplementary Fig. 1b).

We computed field correlations between monthly HCE indices and precipitation and temperature for the Northern Hemisphere (0–80° N), derived from the monthly resolved CRU TS4.01 dataset of gridded (0.5°×0.5°) climate indices. From the field correlation analyses we determined the fraction of the map (%) with significant correlations between monthly HCE with gridded 0.5° CRU TS4.01 temperature and precipitation data (Supplementary Fig. 1a).

These field correlations between monthly HCE indices and precipitation for the Northern Hemisphere (0–80° N) show a high percentage of grid cells with significant correlations for February and March, probably due to intensification of the Hadley circulation during winter and early spring (Supplementary Fig. 1a). HCE movements during winter also have a significant impact on climate (Supplementary Fig. 1a). Field correlations between monthly HCE indices and temperature for the Northern Hemisphere (0–80° N) show the highest percentage of grid cells with significant correlations for December and January. However, in the Northern Hemisphere, tree-ring proxies that capture winter variability are scarce, particularly temperature-sensitive ones. We thus chose early spring as the target season for our reconstruction of the tropical belt northern boundary: that is, HCE averaged from February to April, HCE_{FMA}. The HCE_{FMA} index correlates significantly (positively, $P<0.05$) with the HCE indices of January and summer (July, August and September, Supplementary Table 5).

To assess the influence of interannual HCE variability on Northern Hemisphere climate we developed composite maps for the 10th (southernmost) and 90th (northernmost) percentiles of HCE_{FMA}. Northern Hemisphere climate data included gridded FMA averages of sea level pressure from the 20CR dataset, sea surface temperatures from the HadISST1 dataset, and CRU TS4.01 precipitation data[53]. Field correlation analysis and composite maps were computed using the KNMI Climate Explorer (https://climexp.knmi.nl; ref. [54]).

We calculated Pearson correlation coefficients on an annual basis, from February to April, between our HCE_{FMA} index and the PNA pattern time series from the US National Weather Service Climate Prediction Center (CPC; http://www.cpc.ncep.noaa.gov/) over the period AD 1950–2014, and between HCE_{FMA} index and two ENSO indices (the Central Pacific HadISST1 NIÑO3.4 and the eastern Pacific HadISST1 NIÑO4[55]) and the PDO index time series (http://research.jisao.washington.edu/pdo/PDO.latest.txt, refs [56,57]) over three time windows: 1930–2014, 1943–1978 and AD 1979–2014.

The significance level for field correlations and time series was set to $P<0.05$.

Tree-ring data and climate response of regional chronologies. We selected a network of precipitation or drought-sensitive tree-ring chronologies (Supplementary Table 1) to reconstruct Northern Hemisphere HCE_{FMA} based on three criteria: (1) located in a Northern Hemisphere region that is climatically influenced by HCE_{FMA} (Fig. 1), (2) sensitive to the same FMA climatic variable that is influenced by HCE_{FMA} and (3) statistically significantly correlated with HCE_{FMA} over the period of overlap. Of the 96 chronologies that fit these criteria, 78 were derived from the International Tree-Ring Data Bank (ITRDB; http://www.ncdc.noaa.gov/data-access/paleoclimatology-data/datasets/tree-ring) and 18 additional chronologies were contributed by the authors (Supplementary Table 1). The chronologies are clustered in five regions in W USA and C USA, Turkey (E EU), northern Pakistan (W Asia) and the Tibetan Plateau (C Asia) (Fig. 1, Supplementary Table 1).

For each region, we combined the individual tree-ring series of the contributing chronologies into a regional chronology. Between 6 and 47 site chronologies contributed to each of the five regional chronologies (Supplementary Table 3a). This chronology development approach allows for improved sample depth further back in time and emphasizes the common signal within a region[58]. Between 150 and 2,908 individual tree-ring series were thus compiled per regional chronology (Fig. 2c; Supplementary Table 3a). Age-related trends were removed from the raw measurements of individual tree-ring series using cubic smoothing splines with a 50% frequency-response cut-off equal to 2/3rds of the length of each series (SupplementaryTable 3a). Regional chronologies were then calculated by averaging the detrended series using a biweight robust mean. The variance of each regional chronology was stabilized to avoid biases due to changing in series replication over time[59]. Regional chronologies were then scaled to match their mean and variance with the target HCE_{FMA} time series over the period of overlap (AD 1930–2003). The period spanned reliably by each regional chronology was determined based on the expressed population signal (EPS): the chronology period was cut off for reconstruction when EPS values fell below the commonly used yet arbitrary threshold of 0.85. Using this threshold, all five regional chronologies covered the period AD 1532–2003, and three of the chronologies (W USA, C USA and C ASIA) extended back to AD 1203 (Supplementary Table 3a; Fig. 2c).

We assessed the climate responses for the five regional chronology using Pearson correlation analyses (significance level set to $P<0.05$) with monthly and seasonal precipitation, temperature and scPDSI data for the target months of the HCE reconstruction (February to April and 1- to 2-month combinations thereof), over the period AD 1930–2003. Monthly and seasonal climate data were averaged for all CRU grid points within a region defined by the most distant north–south latitude and east–west longitude coordinates of all the individual chronologies contributing to each regional chronology (Supplementary Table 2). Each of the five regional chronologies correlated significantly with HCE_{FMA} (Supplementary Table 3a) as well as with regional early spring climate variables that are influenced by HCE_{FMA} (Supplementary Table 2). The signs of the correlations between tree-ring chronology and HCE_{FMA} correspond to the signs of the precipitation–HCE_{FMA} correlations for all regions (Fig. 1), suggesting that the statistical link between tree growth and HCE_{FMA} in these regions is founded in HCE and tree-growth climatology.

Reconstruction of the early spring northern boundary of the tropical belt. The five regional chronologies were included in a stepwise multiple linear regression model that was calibrated against the instrumental HCE_{FMA} index over the period AD 1930–2003 (Supplementary Table 3b). This model was used to reconstruct HCE_{FMA} over the period AD 1532–2003—the period common to all five chronologies. We used the split calibration-verification method to determine the skill of the reconstruction over two sub-periods AD 1930–1967 and 1968–2003, where above-zero values of coefficient of efficiency (CE) and reduction of error (RE) statistics indicate that the regression model has acceptable reliability in reproducing the HCE_{FMA} target signal in both sub-periods[60] (Supplementary Table 3c).

Uncertainty in the reconstruction arises from (1) the decreasing number of tree-ring series back through time (replication error) and (2) unexplained variance in the stepwise multiple linear regression model (calibration error; ref. [61]). We estimated the replication error for each regional chronology by bootstrapping[62]: standardized tree-ring measurements for every year were sampled with replacement 1,000 times, and arithmetic means were calculated. Two-tailed 95% confidence intervals (CI) were estimated based on the distribution of the bootstrapped mean and the upper and lower limits of the CI were used as the replication error boundaries. The calibration error was estimated as the standard error (SE) for the full calibration period AD 1930–2003. The overall error of the reconstruction was then estimated as the square root of the standardized summed and squared replication error of each regional master chronology and calibration error terms. The same protocol (including model development, calibration and uncertainty estimation) was used to develop a second HCE_{FMA} reconstruction using only the three regional chronologies that extended back to AD 1203 (Supplementary Fig. 3; Supplementary Table 3c). The two reconstructions were merged to obtain the reconstruction of the early spring tropical belt northern boundary ($RHCE_{FMA}$), with the five-chronology model covering the period AD 1532–2003 and the three-chronology model the period AD 1203–1531 (Fig. 2).

We performed a multi-taper method spectrum analysis[63] to identify the periodicity of the $RHCE_{FMA}$ reconstruction. A wavelet analysis was also performed using a Morlet transform[64] on the full reconstruction to determine whether low-frequency behaviour of the $RHCE_{FMA}$ was stationary over time. Spectrum

and wavelet analyses were performed with KNMI Climate Explorer[54]. Statistical significance was tested (95% confidence intervals) against a red-noise background.

ENSO, PNA and PDO reconstructions. We calculated Pearson correlation coefficients (significance level set to $P<0.05$) on an annual basis between the $RHCE_{FMA}$ and two ENSO reconstructions and one PNA reconstruction over the maximum period of overlap (AD 1203–2003). Weak agreement between various PDO reconstructions for the period prior to the twentieth century[27] prevents us from confirming with confidence past coupling between PDO and $RHCE_{FMA}$. The Central Pacific November through January NIÑO3.4 SST reconstruction[24] is based on tree-ring chronologies from both the tropics and mid-latitudes of both hemispheres and overlaps roughly 10% with chronologies used in the $RHCE_{FMA}$. The eastern Pacific NIÑO4 SST reconstruction[25] is based on tree-ring oxygen isotopic time series from Taiwan. It targets the spring season (March–May) and is independent of the $RHCE_{FMA}$. The winter (December through March) PNA[26] reconstruction is based on 29 proxies from the Northern Hemisphere, and it shares 2 (out of 96) site chronologies with the $RHCE_{FMA}$.

We compared lagged relationships between $RHCE_{FMA}$ and ENSO and PNA reconstructions in an SEA (Fig. 3a–c) using the R package dplR[65]. For this purpose, we superposed an 11-year window of contemporaneous and lagged $RHCE_{FMA}$ anomalies centred over reconstructed positive and negative ENSO and PNA extremes (event years). Positive (negative) event years in the ENSO and PNA reconstructions[24–26] were defined as the 95th and 90th (5th and 10th) percentiles of the reconstructions, after processing with a 10-year high-pass filter to isolate interannual variability (Supplementary Table 6). Monte Carlo simulations ($n=10{,}000$) were used to develop bootstrapped confidence intervals to estimate whether $RHCE_{FMA}$ anomalies were significantly ($P<0.05$) higher or lower than average in the 11-year window ($t-5$ to $t+5$) centred around the ENSO and PNA event years ($t=0$).

To corroborate our results, we also calculated the inverse SEA, in which we determined reconstructed ENSO and PNA anomalies in an 11-year window centred on the southernmost (northernmost) $RHCE_{FMA}$ event years, defined as the 5th (95th) and 10th (90th) percentiles of the $RHCE_{FMA}$, after processing with a 10-year high-pass filter (Supplementary Table 7, Supplementary Fig. 4).

Global volcanic forcing. Newly revised ice-core records of volcanic forcing[29] and two additional independent volcanic forcing reconstructions[66,67] that extend back to at least AD 1203 were used to analyse the response of the reconstruction of the early spring tropical belt northern boundary to major volcanic stratospheric sulfur injection events over the past eight centuries.

We consider major volcanic forcing events those that have either a tropical source (T) or an estimated sulfate injection that was once (1P) or twice (2P) the size of the eruption of Mount Pinatubo in 1991, a commonly used metric of global volcanic forcing equivalent to $-7.5\,W\,m^{-2}$ of volcanic forcing[29], 15 Tg of sulfate aerosols[67] or $11\,kg\,km^{-2}$ of sulfate flux[66] (Supplementary Table 4).

Eruption years, volcano names and regions, and volcanic explosivity index (VEI) of major volcanic forcing events listed by ref. [29] were assigned to known volcanic events. The match of ice-core sulfate signals with volcanic eruptions was mainly based on ref. [68]. Nine out of the 30 volcanic events listed with a tropical source and 6 out of the 14 volcanic events classified as 1P remain unknown. Only 1 out of the 5 volcanic events classified as 2P remain unknown, the volcanic event of 1230. The other four 2P events correspond to the eruptions of Rinjani (Samalas) in 1258, Kuwae in 1458 (ref. [69]), Grímsvötn in 1783 and Tambora in 1815 (Supplementary Table 4).

When ice-core sulfate signals were not matched to a known eruption, eruption latitudes—tropical, Northern Hemisphere or Southern Hemisphere source—were assigned based on the presence or lack of simultaneous signals in both Greenland and Antarctic ice cores. Therefore, synchronous sulfate deposition on both polar ice sheets indicate a tropical eruption, and signals in only one hemisphere are assumed to be extratropical in origin and were attributed accordingly to Northern Hemisphere or Southern Hemisphere eruptions[29].

We conducted SEA to determine the averaged response in degrees of latitude of $RHCE_{FMA}$ to major volcanic forcing events in the 11-year window ($t-5$ to $t+5$) centred around these volcanic events ($t0$). We first used as a list of events the tropical volcanic eruptions (T) and 1P and 2P eruptions from the three volcanic reconstructions[29,66,67] (Supplementary Table 4). Northern Hemisphere and Southern Hemisphere source events were also tested in SEA but not reported because of the lack of significance. To investigate the volcanic response of the five contributing regional chronologies to the early spring tropical belt northern boundary reconstruction, we also ran SEA using as event years the tropical volcanic eruptions (T) and the 1P and 2P eruptions from the volcanic reconstruction of ref. [29].

Data availability

The $RHCE_{FMA}$ will be housed at NOAA-Paleoclimatology/World Data Service for Paleoclimatology: https://www.ncdc.noaa.gov/paleo/study/25050. The data that support the findings of this study are available from the corresponding author upon request.

References

51. Studholme, J. & Gulev, S. Concurrent changes to Hadley circulation and the meridional distribution of tropical cyclones. *J. Clim.* **31**, 4367–4389 (2018).
52. Donat, M. G. et al. Reanalysis suggests long-term upward trends in European storminess since 1871. *Geophys. Res. Lett.* **38**, L14703 (2011).
53. Harris, I., Jones, P. D., Osborn, T. J. & Lister, D. H. Updated high-resolution grids of monthly climatic observations—the CRU TS3.10 Dataset. *Int. J. Climatol.* **34**, 623–642 (2014).
54. Trouet, V. & Van Oldenborgh, G. J. KNMI Climate Explorer: a web-based research tool for high-resolution paleoclimatology. *Tree-Ring Res.* **69**, 3–13 (2013).
55. Rayner, N. A. et al. Global analyses of sea surface temperature, sea ice, and night marine air temperature since the late nineteenth century. *J. Geophys. Res.* **108**, 4407 (2003).
56. Zhang, Y., Wallace, J. M. & Battisti, D. S. ENSO-like interdecadal variability: 1900–93. *J. Clim.* **10**, 1004–1020 (1997).
57. Mantua, N. J., Hare, S. R., Zhang, Y., Wallace, J. M. & Francis, R. C. A Pacific interdecadal climate oscillation with impacts on salmon production. *Bull. Am. Meteorol. Soc.* **78**, 1069–1079 (1997).
58. Trouet, V. A tree-ring based late summer temperature reconstruction (AD 1675–1980) for the Northeastern Mediterranean. *Radiocarbon* **56**, S69–S78 (2014).
59. Frank, D., Esper, J. & Cook, E. R. On variance adjustments in tree-ring chronology development. *Tree Rings Archaeol. Climatol. Ecol. TRACE* **4**, 56–66 (2006).
60. Cook, E. R., Meko, D. M., Stahle, D. W. & Cleaveland, M. K. Drought reconstructions for the continental United States. *J. Clim.* **12**, 18 (1999).
61. Esper, J. et al. Long-term drought severity variations in Morocco. *Geophys. Res. Lett.* **34**, L17702 (2007).
62. Briffa, K. R. et al. Fennoscandian summers from AD 500: temperature changes on short and long timescales. *Clim. Dyn.* **7**, 111–119 (1992).
63. Jenkins, G. & Watts, D. Spectral analysis and its applications. *Louvain Econ. Rev.* **36**, 554–554 (1970).
64. Torrence, C. & Compo, G. P. A practical guide to wavelet analysis. *Bull. Am. Meteorol. Soc.* **79**, 61–78 (1998).
65. Bunn, A. G. A dendrochronology program library in R (dplR). *Dendrochronologia* **26**, 115–124 (2008).
66. Crowley, T. J. & Unterman, M. B. Technical details concerning development of a 1200 yr proxy index for global volcanism. *Earth Syst. Sci. Data* **5**, 187–197 (2013).
67. Gao, C., Robock, A. & Ammann, C. Volcanic forcing of climate over the past 1500 years: an improved ice core-based index for climate models. *J. Geophys. Res.* **113**, D23111 (2008).
68. Sigl, M. et al. A new bipolar ice core record of volcanism from WAIS Divide and NEEM and implications for climate forcing of the last 2000 years. *J. Geophys. Res. Atmospheres* **118**, 1151–1169 (2013).
69. Plummer, C. T. et al. An independently dated 2000-yr volcanic record from Law Dome, East Antarctica, including a new perspective on the dating of the 1450s CE eruption of Kuwae, Vanuatu. *Clim. Past* **8**, 1929–1940 (2012).